In-situ neutron diffraction during stress relaxation of a single crystal nickel-base superalloy

Collins, David; D'Souza, Neil; Panwisawas, Chinnapat

DOI:
10.1016/j.scriptamat.2017.01.002

Document Version
Publisher's PDF, also known as Version of record

Citation for published version (Harvard):
Collins, D, D'Souza, N & Panwisawas, C 2017, 'In-situ neutron diffraction during stress relaxation of a single crystal nickel-base superalloy', Scripta Materialia, vol. 131, pp. 103-107.
https://doi.org/10.1016/j.scriptamat.2017.01.002

Scripta Materialia 131 (2017) 103–107

Contents lists available at ScienceDirect

Scripta Materialia

journal homepage: www.elsevier.com/locate/scriptamat

Regular Article

In-situ neutron diffraction during stress relaxation of a single crystal nickel-base superalloy

David M. Collins[a], Neil D'Souza[b], Chinnapat Panwisawas[c]

[a]Department of Materials, University of Oxford, Parks Road, Oxford OX1 3PH, UK
[b]Rolls-Royce plc, PO. Box 31, Derby DE24 8BJ, UK
[c]School of Metallurgy and Materials, University of Birmingham, Edgbaston, Birmingham B15 2TT, UK

ARTICLE INFO

Article history:
Received 24 October 2016
Received in revised form 24 December 2016
Accepted 3 January 2017
Available online 26 January 2017

Keywords:
Superalloys
Neutron diffraction
Single crystal
Stress relaxation
Lattice strain

ABSTRACT

The stress relaxation behaviour of a single crystal nickel-base superalloy has been quantified using time-of-flight neutron diffraction analysis for a range of temperatures relevant to casting. A new iterative analysis methodology is described to isolate the lattice strain behaviour of the γ matrix and γ' precipitate phases from data obtained sufficiently rapidly to help elucidate the microscopic effect of macroscopic stress relaxation. The independent response of γ and γ' is revealed, showing the temperature sensitivity of lattice strain relaxation. The γ/γ' response is discussed in the context of thermo-mechanical conditions that may affect the propensity for recrystallisation.

Nickel-base superalloys are typically chosen for turbine blade applications due their excellent high temperature mechanical and environmental properties. To confer suitable creep performance, the material is cast into a single crystal via directional solidification, involving a controlled mould withdrawal from the furnace. During this process, macroscopic residual stresses are produced in the component due to localised plastic flow induced from the different thermal expansions of the metal and the ceramic mould during cooling. These are sufficient for the metal to experience visco-plasticity through creep and stress relaxation, affecting the resultant dislocation density. This has implications to recrystallisation during subsequent processing heat treatments. Such artifacts are unacceptable during turbine blade manufacture. It is therefore critical to quantify macromechanical and micromechanical strains, in addition to their sensitivity to processing conditions.

An attractive method for quantifying micromechanical strains in nickel-base superalloys is diffraction via the evaluation of lattice strains. In particular, techniques that offer high angular resolution to separate the disordered A1 γ matrix and ordered $L1_2$ structured γ' precipitates are desirable. Experiments are often complicated by the desire to obtain information at service or processing relevant stresses and/or temperatures. Laboratory X-ray sources can be equipped with in-situ testing capability, though their low flux and energy typically prohibits the measurement of the inherently weak γ' superlattice reflections. Experiments are instead commonly performed at either synchrotron or neutron sources. To date, experimenters have investigated dynamic behaviour such as tensile [1,2], creep [3–5], processing heat treatments & phase transformations [6–9] and stress relaxation [10,11]. In this study, an analysis methodology is developed that enables quantification of γ and γ' lattice strains to investigate the stress relaxation behaviour in-situ during time-of-flight neutron diffraction measurements of a single crystal nickel-base superalloy. With a necessarily rapid data acquisition time to describe such phenomena, the new method enables analysis of diffraction data with a low signal to noise ratio that would be impossible using existing data fitting strategies.

As-cast cylindrical single crystal specimens of CMSX-4 nickel-base superalloy (Ni–5.6Al–9.0Co–6.5Cr–0.6Mo–3.0Re–6.5Ta–6.0W–0.1Hf, wt.%) were studied. Each specimen had a 5.85 mm diameter and 29 mm gauge length. They were processed and machined using conditions described in [11,12].

Time-of-flight diffraction experiments were performed on the ENGIN-X neutron diffractometer [13], ISIS, UK. The experimental setup adopted during the acquisition of neutron diffraction data is shown in Fig. 1. The neutron signal was obtained from a probed volume measuring $8 \times 4 \times 4$ mm^3, controlled by the incident beam cross section and the collimator size. Samples were heated in an optical furnace at 10 °C min^{-1} to 800 °C then at 5 °C min^{-1} to the test temperatures 900 °C, 940 °C, 980 °C and 1000 °C measured with a K-type thermocouple, followed by a 20 min hold period before

http://dx.doi.org/10.1016/j.scriptamat.2017.01.002

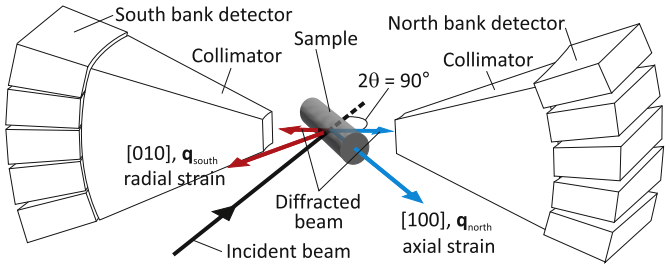

Fig. 1. Schematic illustration of the experimental setup on the ENGIN-X instrument at ISIS, Didcot, UK.

loading. Using a tensile rig on the beam line, four specimens were loaded at a strain rate of 3.3×10^{-5} s^{-1} to different initial stress levels (600 MPa, 480 MPa, 400 MPa and 380 MPa). Stresses were held at these magnitudes under load control for 9 min. Thereafter, relaxation was conducted under displacement control for 9 min. The load, hold and relaxation cycle was repeated for 6–7 cycles, with each cycle increasing the macroscopic stress by 10 MPa.

The measurement of γ and γ' lattice parameters has been achieved by adopting a new data fitting strategy, developed from a previous methodology used for the analysis of X-ray diffraction data from polycrystalline nickel-base superalloys [9]. This method is tailored for time-of-flight neutron diffraction data from single crystal superalloys, incorporating the characteristic line profile asymmetry arising from the thermalisation process of neutrons, producing a time distribution of the neutron pulse [14]. The line profile shape used is a convolution product of a Voigt function and a trailing exponential function, where the former is defined as

$$V(x) = G(x) \otimes L(x) \tag{1}$$

where $V(x)$ is the Voigt function, $G(x)$ is the Gaussian function, $L(x)$ is the Lorentzian function. The independent variable is $x = d - d_c$ where d is d-spacing converted from time-of-flight and d_c is the d-spacing coordinate of the peak centre of mass. The full fitting function, $V_{exp}(x)$, is given by

$$V_{exp}(x) = V(x) \otimes \exp(-\eta x)H(x) \tag{2}$$

where η is a constant and $H(x)$ is the Heaviside step function. The line profile asymmetry from the ENGIN-X instrument was determined by performing single peak fitting (using V_{exp} function) of a CeO_2 standard on all reflections in the d-spacing range 1.19 Å $< d <$ 2.88 Å.

To correctly fit the superalloy diffraction patterns, the parameters contributing to the intensity of individual reflections are considered. Following [15], the integrated intensity, I of a polychromatic incident neutron beam for a single Laue spot is

$$I \propto \frac{I_0(\lambda_0)\lambda_0^4 |F_{khl}|^2}{2\sin^2\theta_0} \frac{\Delta v}{v_a^2} \tag{3}$$

where $I_0(\lambda_0)$ is the intensity-wavelength (λ_0) distribution, F_{hkl} is the structure factor for reflection hkl, Δv is the diffracted volume, v_a is the unit cell volume and θ_0 is the Bragg angle. For the fundamental {200} reflections (example (200) reflection shown in Fig. 2b), the measured intensity is the superposition of intensity from the γ (I^{γ}_{200}) and γ' ($I^{\gamma'}_{200}$) phases. As the γ/γ' lattice misfit for CMSX-4 is

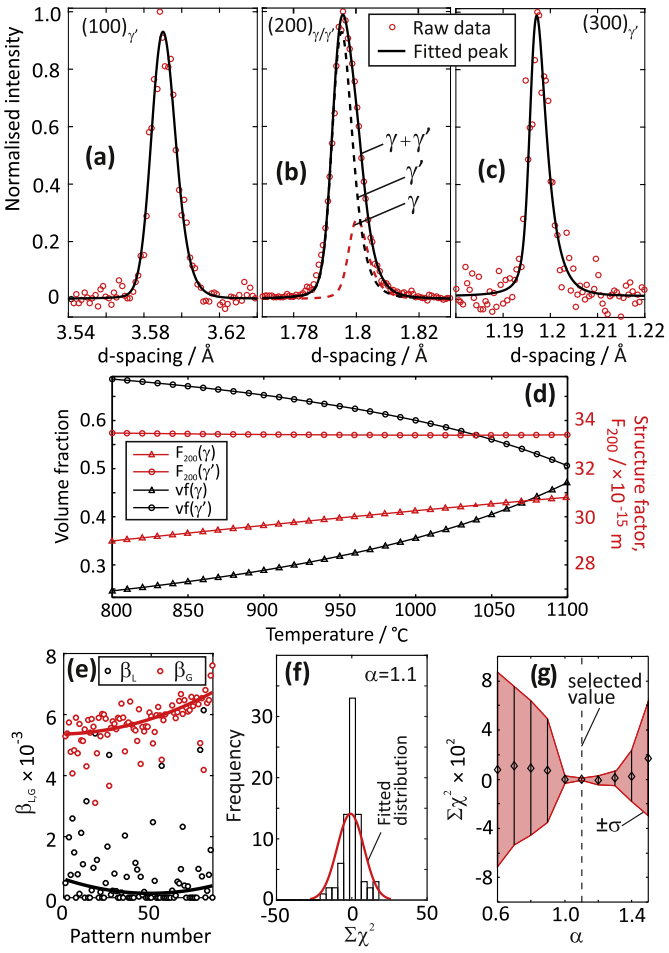

Fig. 2. Example diffraction reflections collected at 20 °C with no stress applied for (a) the superlattice (100) (b), fundamental (200), (c) superlattice (300), (d) predictions of γ & γ' volume fractions and calculated {200} γ & γ' structure factors, (e) fitted $(200)_{\gamma}$ Lorentzian breadth (β_L) and Gaussian breadth (β_G), (f) fitted distribution of $\Sigma\chi^2$ errors for all patterns obtained from a sample, and (g) the effect of α on $\Sigma\chi^2$.

small, (typically -5×10^{-3} to 1×10^{-3} [16,17]) Eq. (3) can be used to express the ratio of intensity between the two reflections:

$$\frac{I^{\gamma}_{200}}{I^{\gamma'}_{200}} = \frac{|F^{\gamma}_{200}|^2}{|F^{\gamma'}_{200}|^2} \frac{\Delta v^{\gamma}}{\Delta v^{\gamma'}} \tag{4}$$

All absent terms from Eq. (3) are eliminated, being equivalent for γ and γ' (including unit cell volumes where $v_a^{\gamma} \approx v_a^{\gamma'}$). Whilst the above intensity expression has been simplified; neglecting absorption, extinction and thermal vibration effects is valid as their contributions are approximately cancelled in Eq. (3). For the $(200)_{\gamma}$ reflection, the structure factor (simplified from general expressions, described elsewhere [9]) is

$$F^{\gamma}_{200} = 4\sum c_Z b_Z \tag{5}$$

where c_Z is the composition and b_Z is the bound coherent scattering length for each element, Z, with terms for the latter tabulated in [18]. For the ordered $L1_2$ structured γ' with a Ni_3Al stoichiometry, the (200) fundamental reflection structure factor is

$$F^{\gamma'}_{200} = 3\sum_A c_{Z_A} b_Z + \sum_B c_{Z_B} b_Z \tag{6}$$

where an element Z may be present on a 'Ni' site, A or 'Al' site, B. Their respective site occupancies are c_{Z_A} and c_{Z_B}. CMSX-4 possesses a strong elemental partitioning to a single γ' site, except Cr which has a composition dependent site preference [19]. The present study assumes Ni and Co occupy site A, whilst all remaining elements including Cr are occupant on the B site. Following a prediction of equilibrium temperature dependent phase compositions using the thermodynamic calculation tool, JMatPro [20], γ compositions were used in Eq. (5) and γ' compositions were used to evaluate γ' site occupancies, and the terms c_{Z_A} and c_{Z_B} in Eq. (6). The γ' composition is not predicted nor measured experimentally [21] to change dramatically as a function of temperature, hence, Cr is not expected to switch site preference. Phase equilibria calculations provide γ & γ' volume fractions, shown in Fig. 2 (d). These values along with calculated structure factor values (shown in Fig. 2 (d)) were used to evaluate the γ/γ' intensity ratio in Eq. (4).

All analysis and fitting functions were written in Matlab using the following methodology:

1. Determine the instrumental contribution to line profile asymmetry, with a parameter denoted η, from fitted CeO_2 reflections. Obtain an empirical function of asymmetry by fitting a polynomial to η values as a function of d-spacing. Values of η are calculated from this polynomial for all subsequent reflection fitting.
2. Fit the normalised $\{100\}_{\gamma'}$ and $\{300\}_{\gamma'}$ superlattice reflections independently using Eq. (2).
3. Infer the position of $\{200\}_{\gamma'}$ from the superlattice reflection positions, described previously [22], here given as $d^{\gamma'}_{200} = \frac{1}{2}\left(\frac{1}{2}d^{\gamma'}_{100} + \frac{3}{2}d^{\gamma'}_{300}\right)$.
4. Obtain the $\{200\}_{\gamma'}$ line profile shape by interpolating the Gaussian and Lorentzian widths, β^L & β^G respectively, from the $\{100\}$ and $\{300\}$ superlattice reflections with respect to d-spacing. This width is equivalent to $\beta^{L,G}_{200} = \frac{\alpha}{4}\left(3\beta^{L,G}_{300} + \beta^{L,G}_{100}\right)$. The constant, α, is refined later, fixed now at 1.
5. Introduce a scale factor, A, for the $\{200\}_{\gamma'}$ peak to give $I^{\gamma'}_{200} = AV_{\text{exp}}$. From an arbitrary guess of A, the γ intensity from the total intensity of the fundamental reflection, I_{200}, is calculated using $I^{\gamma}_{200} = I_{200} - AV_{\text{exp}}$. Adopting an iterative scheme such as the bisection method, the magnitude of A was varied until the $I^{\gamma}_{200}/I^{\gamma'}_{200}$ ratio in Eq. (4) is satisfied.
6. The intensity, I^{γ}_{200}, is normalised and fitted with the V_{exp} function. The position of d^{γ}_{200} is obtained.
7. Repeat steps 2–6 for all diffraction spectra, recording β_L and β_G. Fit these parameters with respect to pattern number as shown in Fig. 2 (e). Repeat the fitting of all spectra using fitted β_L & β_G values.
8. The peak width scaling parameter α is now refined. The fitting error of the $\{200\}_{\gamma,\gamma'}$ fundamental reflections are calculated for all patterns in a test using the χ^2 Pearson's cumulative test statistic. A histogram of these errors summed $\Sigma\chi^2$ was fitted with a normal distribution, as shown in Fig. 2 (f). Repeat steps 2–7, using different α values (0.6 to 1.6 used here). The selected value of α has the narrowest $\Sigma\chi^2$ distribution close to zero. The variation of $\Sigma\chi^2$ with α is shown in Fig. 2 (g).

Example raw data at room temperature with no stress applied is shown in Fig. 2 with fitted (100) and (300) superlattice reflections in (a) and (c), respectively. A fitted fundamental (200) reflection is shown in (b), with the separated γ and γ' intensity contributions.

The influence of introducing fitting constraints on a_γ, $a_{\gamma'}$ and $\Sigma\chi^2$ error (from the fitted I_{200} peak) is shown in Fig. 3. Method A is the benchmark fitting procedure; adopting a $V(x)$ line profile shape and fixing $d^{\gamma'}_{200}$ from the fitted superlattice reflection position. Here, the parameters d^{γ}_{200}, the overall intensities and widths of each peak

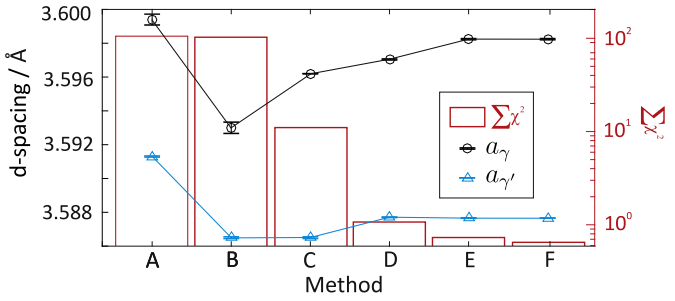

Fig. 3. Variation of $a_{\gamma'}$, a_γ and I_{200} fitting error ($\Sigma\chi^2$) by increasing the number of fitting constraints (between models A to F) for data obtained at 20 °C with no stress applied.

and background are free variables, similar to the method described in [16]. Method B uses a $V_{\text{exp}}(x)$ line profile shape, Method C adds the $I^{\gamma}_{200}/I^{\gamma'}_{200}$ ratio constraint (described in step 5 above), Method D adds a constraint to η for all reflections (step 1), Method E uses fitted values of β_G & β_L (step 7), and Method F includes the refined parameter α (step 8). Values of $\Sigma\chi^2$ from I_{200} indicate the success of the fitted reflection; each constraint added between Methods A to F improves the fit. Lattice parameters a_γ and $a_{\gamma'}$ are affected by the fitting constraints; converging to correct values as $\Sigma\chi^2$ becomes small. Adopting Method F does not invalidate Method A, however, such procedures are only suitable for data with sufficiently high signal to noise ratio. For rapid data acquisition, as considered here, a more robust analysis routine, i.e. Method F, must be adopted.

The material response to the stress relaxation experiment for the range of tested temperatures as a function of time is shown in Fig. 4. Maps of measured intensity are shown in the first column (a) for the d-spacing range close to the {200} reflections in the [100] and [010] directions. No data was collected in the [010] direction at 940 °C. Thermal expansion during heating provides the increased d-spacing during the first ~100 min. Superimposed plots of macroscopic stress are also shown. Qualitatively, the red-yellow regions of high intensity correspond to the positions of the γ and γ' {200} fundamental reflections. The serration periodicity observed in this data follows the macroscopic loading-relaxation pattern.

The fitting procedure described earlier was used to calculate the γ and γ' lattice parameters, as shown in column 2 (b). Lattice strains were next calculated, column 3 (c), where $\epsilon^{\gamma,\gamma'}_{200}$ ([100] direction) was obtained from

$$\epsilon^{\gamma,\gamma'}_{200} = \frac{d^{\gamma,\gamma'}_{200} - d^{\gamma,\gamma'}_{200}(\sigma = 0)}{d^{\gamma,\gamma'}_{200}(\sigma = 0)} \tag{7}$$

where $d^{\gamma,\gamma'}_{200}(\sigma = 0)$ is the reference d-spacing prior to the first load cycle at the test temperature, and $d^{\gamma,\gamma'}_{200}$ is the measured d-spacing during the stress relaxation test at the same temperature. For $\epsilon^{\gamma,\gamma'}_{020}$, Eq. (7) values of $d^{\gamma,\gamma'}_{200}$ & $d^{\gamma,\gamma'}_{200}(\sigma = 0)$ are replaced with $d^{\gamma,\gamma'}_{020}$ & $d^{\gamma,\gamma'}_{020}(\sigma = 0)$. The lattice strain responses are annotated in Fig. 4 (d) to identify features in the γ/γ' relaxation behaviour. These are herewith used for discussion.

During the stress relaxation cycles in the [100] tensile direction at 900 °C, $a_{\gamma'}$ and a_γ are quite similar compared to 1000 °C where $a_{\gamma'}$ remains greater than a_γ whilst at 900 °C $a_{\gamma'}$ and a_γ are quite similar. This corroborates with experimental evidence [23] that dislocation flow in γ is preferred at 1000 °C. As the lattice misfits prior to loading does not vary for the tested temperatures, a smaller difference between $\epsilon^{\gamma'}_{(200)}$ and $\epsilon^{\gamma}_{(200)}$ is observed at 1000 °C compared to 900 °C. Following a load hold, the $\epsilon^{\gamma'}_{(200)}$ decay rate is higher than $\epsilon^{\gamma}_{(200)}$, becoming more obvious for cycles 6–7. For all temperatures,

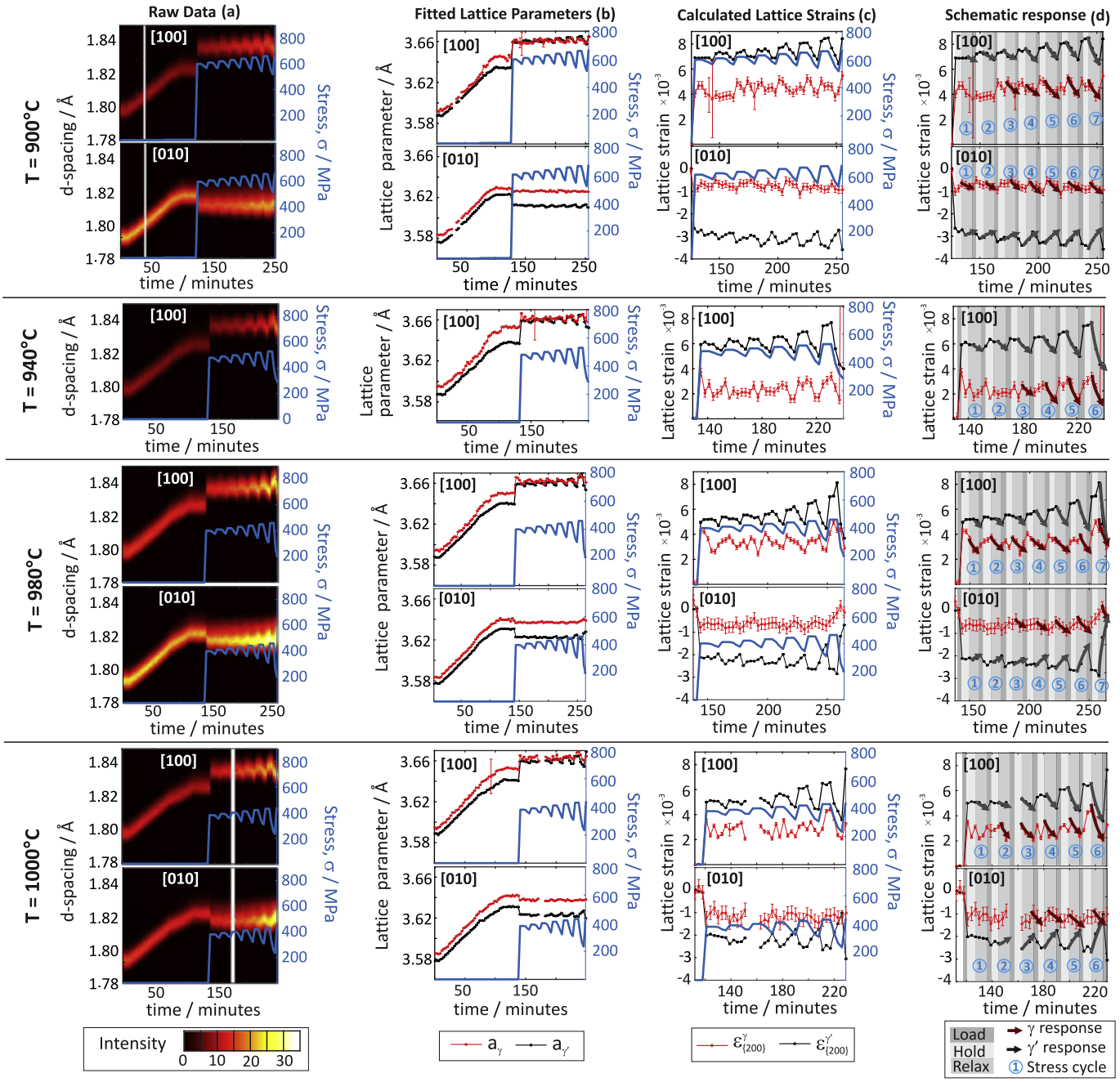

Fig. 4. Temperature and time dependent stress relaxation diffraction analysis results in the [100] and [010] directions. (a) Measured intensities of the $\{200\}_{\gamma/\gamma'}$ reflection are shown as colour maps. (b) Fitted γ & γ' lattice parameters, (c) calculated γ & γ' {200} reflection lattice strains as a function of time are shown and, (d) annotated results.

the difference between $\epsilon^{\gamma}_{(200)}$ and $\epsilon^{\gamma}_{(200)}$ reduces after each successive cycle.

In the transverse [010] direction, for all temperatures, $\epsilon^{\gamma}_{(020)}$ and $\epsilon^{\gamma'}_{(020)}$ exhibit compressive lattice strains when the tensile load is applied. When the macroscopic stress is relaxed, $\epsilon^{\gamma}_{(020)}$ increases whilst $\epsilon^{\gamma}_{(020)}$ decreases, hence their strain difference between them reduces. At 900 °C the lattice strain is always higher in γ than γ' by $\sim 3\times10^{-3}$ during the hold period and $\sim 1.6\times10^{-3}$ after the relaxation period. The difference between $\epsilon^{\gamma}_{(020)}$ and $\epsilon^{\gamma'}_{(020)}$ reduces significantly with increasing temperature. By the final stress relaxation cycle at 1000 °C, their magnitudes are approximately equal.

Considering recrystallisation, the temperature dependent relative strengths of γ and γ' must play a role. At 1000 °C, γ' is considered undeformable [23], giving a high dislocation density in the γ channels, and thus a high driving force for recrystallisation. However, during relaxation at 1000 °C in this study, $\epsilon^{\gamma'}_{(200)}$ changes are significant and does not support the observation that γ' is undeformable. The magnitude of lattice strain change during relaxation at 1000 °C for γ and γ' is greater than at a lower temperatures; this is significant considering the applied macroscopic stress was lower. The drops in the tensile direction lattice strains, for example, provides evidence that more stored elastic strain energy is released at increased temperatures. How the relaxation of γ' is coupled to

the deformation of γ, however, remains unclear. It is likely that the precipitates themselves are subjected to dislocation cutting [12] and/or experience elastic relaxation due to the plastic deformation of the surrounding γ. This temperature dependent phase selectivity for deformation is likely to determine the propensity for recrystallisation and the future selection of turbine blade solidification processes.

Acknowledgments

The authors acknowledge the allocation of beam time (RB10505) at ISIS, Rutherford Appleton Laboratory, funded by the Science and Technology Facilities Council. With thanks to Dr Joe Kelleher for experimental support. Datasets from this manuscript will be made available via the Oxford University Research Archive (ora.ox.ac.uk).

References

[1] J. Coakley, D. Dye, Scr. Mater. 67 (2012) 435–438.
[2] M.R. Daymond, M. Preuss, B. Clausen, Acta Mater. 55 (2007) 3089–3102.
[3] A. Royer, P. Bastie, M. Veron, Acta Mater. 46 (1998) 5357–5368.
[4] S. Ma, D. Brown, M.A.M. Bourke, M.R. Daymond, B.S. Majumdar, Mater. Sci. Eng. A 399 (2005) 141–153.
[5] J. Coakley, R.C. Reed, J.L. Warwick, K.M. Rahman, D. Dye, Acta Mater. 60 (2012) 2729–2738.
[6] D. Collins, L. Yan, E. Marquis, L. Connor, J. Ciardiello, A. Evans, Acta Mater. 61 (2013) 7791–7804.
[7] L.D. Connor, H.J. Stone, D.M. Collins, M. Preuss, M.C. Hardy, C.M.F. Rae, Metall. Mater. Trans. A 45 (2014) 2436–2444.
[8] G. Bruno, H.C. Pinto, Mater. Sci. Technol. 19 (2013) 567–572.
[9] D. Collins, D. Crudden, E. Alabort, T. Connolley, R. Reed, Acta Mater. 94 (2015) 244–256.
[10] J. Rolph, A. Evans, A. Paradowska, M. Hofmann, M. Hardy, M. Preuss, C. R. Phys. 13 (2012) 307–315.
[11] N. D'Souza, J. Kelleher, C. Qiu, S.Y. Zhang, S. Gardner, R.E. Jones, Acta Mater. 106 (2016) 322–332.
[12] C. Panwisawas, H. Mathur, J.C. Gebelin, D. Putman, C.M. Rae, R.C. Reed, Acta Mater. 61 (2013) 51–66.
[13] J. Santisteban, M. Daymond, J. James, L. Edwards, J. Appl. Cryst. 39 (2006) 812–825.
[14] S. Ikeda, Carpenter, J.M., Nucl. Instrum. Methods A 239 (1985) 536–544.
[15] B. Buras, K. Mikke, B. Lebech, J. Leciejewicz, Phys. Status Solidi 11 (1965) 567–573.
[16] D. Dye, J. Coakley, V. Vorontsov, H. Stone, R. Rogge, Scr. Mater. 61 (2009) 109–112.
[17] R. Völkl, U. Glatzel, M. Feller-Kniepmeier, Acta Mater. 46 (1998) 4395–4404.
[18] V. Sears, Neutron News 3 (1992) 26–37.
[19] H. Murakami, Y. Saito, H. Harada, in: R. Kissinger, D. Deye, A. Cetel, M. Nathal, T. Pollock, D. Woodford (Eds.), Superalloys 1996, TMS, Seven Springs, PA, USA, 1996, pp. 249–257.
[20] S. Software, JMatPro™, Ni Module (v. 2.0), 2002.
[21] F. Pyczak, S. Neumeier, M. Göken, Mater. Sci. Eng. A 527 (2010) 7939–7943.
[22] H. Stone, T. Holden, R. Reed, Acta Mater. 47 (1999) 4435–4448.
[23] D.C. Cox, B. Roebuck, C.M.F. Rae, R.C. Reed, Mater. Sci. Technol. 19 (2002) 440–446.